CHAPTER 7

2D and 3D Image Analysis by Gaussian–Hermite Moments

Bo Yang, Tomas Suk, Mo Dai and Jan Flusser

This chapter introduces 2D and 3D Gaussian–Hermite moments and rotation invariants constructed from them. Thanks to their numerical stability, Gaussian–Hermite moments provide better reconstruction and recognition power than the geometric and most of other orthogonal moments while keeping the simplicity of design of the invariants. This is illustrated by experiments on real 2D and 3D data.

7.1 Introduction

Although moments have been used in many image analysis tasks and areas, probably their most important and most frequent application is in object recognition. The key

Bo Yang, Tomas Suk, Jan Flusser
Institute of Information Theory and Automation of ASCR
182 08 Prague 8, Czech Republic
e-mail: {yang, suk, flusser}@utia.cas.cz

Mo Dai
ENSEGID, Institut Polytechnique de Bordeaux 1
Allee Daguin, 33607 Pessac Cedex, France
e-mail: Mo.DAI@ipb.fr

point is to find descriptors that can represent the object regardless of certain trans-
formations and/or deformations. Moment invariants were proved to be very powerful
tools for feature representation and it has been demonstrated many times that moment
invariants perform effectively in object recognition [7].

So far, various kinds of moment invariants to spatial transformations of the object
have been proposed. Among all transformations that have been studied in this context,
rotation plays a central role. Being a part of rigid-body transformation, object rotation
is present almost in all applications, even if the imaging system is well set up and the
experiment has been prepared in a laboratory. On the other hand, rotation is not trivial
to handle mathematically, unlike for instance translation and scaling. For these two
reasons, invariants to rotation have been in focus of researchers since the beginning.

The development of rotation invariants in 2D space has a long history. As early
as in 1962, Hu first derived seven rotation invariants that formed an incomplete and
dependent system [12]. After Hu, various approaches to the theoretical derivation of
moment-based rotation invariants were published. Li employed Fourier-Mellin trans-
formation to derive rotation invariants up to order nine [17]. Wong et al., on the
other hand, derived the rotation invariants up to order five based on the theory of
algebraic invariants [31]. Flusser offered the solution for complete and independent
set constructed from complex moments [5]. Zernike moments were also considered
for developing rotation invariants. Khotanzad and Hong pointed out that magnitudes
of Zernike moments possess rotation invariance [16]. Wallin and Kubler formulated
an approach to derive a complete set of rotation invariants from Zernike moments
[29]. Some other polynomial bases (Legendre, Krawtchouk, Gaussian–Hermite) were
employed in a similar manner [10, 37, 36].

With the rapid progress of applied mathematics, computer science and sensor tech-
nology, 3D imaging comes into engineering and practice. Undoubtedly, developing
rotation invariants for 3D images has become a hot topic in the computer vision com-
munity. However, 3D rotation is more difficult to handle than its 2D counterpart,
since it has three independent parameters. That is probably why only few papers on
3D rotation moment invariants have appeared so far. The first attempts to derive
3D rotation moment invariants are relatively old. Sadjadi and Hall explored ternary
quadratics extensively and derived three translation, rotation and scaling (TRS) mo-
ment invariants. Their derivation was accomplished by using the invariant properties
of the coefficients in a ternary form [24]. Guo proved Sadjadi and Hall's results in
the different way and he derived more invariants to translation and rotation in 3D
space [9]. Cyganski and Orr applied tensor theory to derive 3D rotation invariants
[2]. This method was also mentioned by [23], who used invariant image features to
recognize planar objects. Xu and Li developed the invariants in both 2D and 3D space
based on geometric primitives such as distance, area, and volume [32]. Galvez and
Canton [8] and Canterakis [1] employed normalization approaches for constructing 3D
moment invariants, which overcame the necessity of an explicit deriving the invariants
but introduced potential numerical instability. Another method to derive 3D rota-
tion invariants is based on complex moments [18, 6]. Several application papers were
published, for example [19], where the authors used 3D TRS invariants for tests of
handedness and sex from MRI snaps of brains as well as two other papers [14] and
[28] discussing utilization of invariants in registration. Most recently, [26] proposed an

automatic algorithm to generate 3D rotation invariants from geometric moments up to an arbitrary order.

Although moments are probably the most popular 3D shape descriptors, it should be mentioned that they are not the only features providing rotation invariance. For example, Kakarala and Mao used the bispectrum, well-known from statistics for feature computation [13]. Kazhdan used an analogy of phase correlation based on spherical harmonics for comparison of two objects [14]. In this particular case it was used for registration, but can be also utilized for recognition. In [15], the authors used amplitude coefficients as the features. Fehr used the power spectrum and bispectrum computed from a tensor function describing an object composed of patches [3]. In [4] the same author employed local binary patterns and in [25] he used local spherical histograms of oriented gradients.

There have been numerous discussions what kind of moments (i.e. what polynomial basis) provide the best performance. The criteria could be discrimination and reconstruction power, robustness to noise, computational efficiency, and also suitability and accessibility for theoretical considerations. Traditional geometric and complex moments are excellent for theoretical analysis but their numerical properties are not optimal. On the other hand, the main advantage of orthogonal moments is their better numerical stability, limited range of values and existing recurrent relations for their calculation. Note that there is no difference from theoretical point of view because any two polynomial bases of the same degree are equivalent. Hence, several authors have tried to derive the 2D invariants from orthogonal moments. In 3D, however, the situation is more difficult than in 2D, but one can still expect that 3D orthogonal moments preserve their favorable numerical properties.

Both in 2D and 3D, there exist polynomials orthogonal inside a unit ball and others that are orthogonal on a unit cube. Seemingly, the polynomials defined on a unit ball are more convenient for deriving rotation invariants because the ball is mapped onto itself and the polynomials are transformed relatively easily under rotation. The invariance is achieved by proper phase cancellation. The most popular basis of this kind is the Zernike basis. However, real images coming from CT and MRI are defined on a cube and must be mapped into a unit ball before the moments are calculated. Such mapping requires resampling which always lead to a loss of precision.

Polynomial system orthogonal on a cube is (mostly but not necessarily) a product of three 1D polynomials. Since 1D orthogonal polynomials can be evaluated by efficient recurrent formulas, we can expect good numerical stability. On the other hand, derivation of invariants is in general very difficult, because the basis polynomials are transformed in a complicated way under rotation.

In this chapter we show that Gaussian–Hermite moments could be a good choice. Gaussian–Hermite basis is orthogonal on a cube which implies good numerical properties. At the same time, Gaussian–Hermite polynomials are transformed under rotation in the same way as the monomials $x^p y^q$. Thanks to this, the respective rotation invariants have the same forms as the rotation invariants from geometric moments. Under our knowledge, Gaussian–Hermite polynomials are the only ones showing this property. This is an important conclusion valid in both 2D and 3D which allows us to reduce rotation invariant derivation from Gaussian–Hermite moments to that from geometric moments, which is much easier to accomplish but we still benefit from the

numerical stability of Gaussian–Hermite moments.

The chapter is organized as follows. First we introduce Gaussian–Hermite polynomials and moments. Then we formulate the central Theorem on the form of Gaussian–Hermite rotation invariants in 2D and 3D. Finally, we demonstrate the invariance property and the discrimination power on simulated as well as real 2D and 3D data.

7.2 Gaussian–Hermite Moments

Before we discuss Gaussian–Hermite moments, it is necessary to introduce Hermite polynomials firstly. Hermite polynomials are orthogonal polynomials defined on the interval $(-\infty, \infty)$

$$H_p(x) = (-1)^p \exp{(x^2)} \frac{d^p}{dx^p} \exp{(-x^2)}. \tag{7.1}$$

It can be efficiently computed by the following 3-term recurrence relation

$$H_{p+1}(x) = 2x H_p(x) - 2p H_{p-1}(x) \quad \text{for } p \geq 1, \tag{7.2}$$

with the initial conditions $H_0(x) = 1$ and $H_1(x) = 2x$. Hermite polynomials are orthogonal when weighted by a Gaussian function

$$\int_{-\infty}^{\infty} H_p(x) H_q(x) \exp{(-x^2)} dx = 2^p p! \sqrt{\pi} \delta_{pq}, \tag{7.3}$$

where δ_{pq} is the Kronecker delta. The basis functions we use for the definition of Gaussian–Hermite moments are normalized versions of Hermite polynomials. Hermite polynomials are scaled and modulated by a Gaussian

$$\hat{H}_p(x; \sigma) = \frac{1}{\sqrt{2^p p! \sqrt{\pi} \sigma}} H_p\left(\frac{x}{\sigma}\right) \exp\left(-\frac{x^2}{2\sigma^2}\right). \tag{7.4}$$

The scaling parameter σ is common to both factors. Figure 7.1 shows the basis functions of orders 0 up to order 5. Obviously, Eq.(7.4) is not only orthogonal but also orthonormal, which means that

$$\int_{-\infty}^{\infty} \hat{H}_p(x; \sigma) \hat{H}_q(x; \sigma) dx = \delta_{pq}. \tag{7.5}$$

Given any image function $f(x, y)$ its Gaussian–Hermite moments are therefore defined as

$$\eta_{pq} = \int_{-\infty}^{\infty} \int_{-\infty}^{\infty} \hat{H}_p(x; \sigma) \hat{H}_q(y; \sigma) f(x, y) dx dy. \tag{7.6}$$

For a 3D image $f(x, y, z)$, its Gaussian–Hermite moments are computed directly by

$$\eta_{pqr} = \int_{-\infty}^{\infty} \int_{-\infty}^{\infty} \int_{-\infty}^{\infty} \hat{H}_p(x; \sigma) \hat{H}_q(y; \sigma) \hat{H}_r(z; \sigma) f(x, y, z) dx dy dz. \tag{7.7}$$

Discrete implementation of Gaussian–Hermite moments is mainly focused on the discretization of the basis functions. Here we only discuss the 1D case. The results
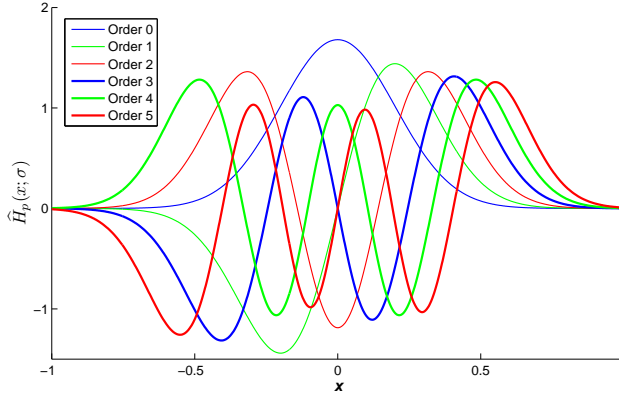
Figure 7.1: The basis functions of Gaussian–Hermite moments of orders 0 up to 5 with $\sigma = 0.20$.

can be directly extended to 2D, 3D and any high–dimension spaces because the basis functions in high–dimension spaces are the products of several basis functions in 1D case.

In the discrete case, the signal $I(i)$ is of a finite length K ($0 \leq i \leq K - 1$). In order to select a meaningful scale parameter σ, we map the signal into $[-1 \leq x \leq -1]$ by setting

$$x = \frac{2i - K + 1}{K - 1}. \tag{7.8}$$

This transformation results in the change of integration variables and introduces a normalization coefficient $\sqrt{2/(K-1)}$. So considering this coefficient and together with Eq.(7.4), we can get the values of basis function corresponding to a signal of length K:

$$\hat{H}_p(i, K; \sigma) = \frac{1}{\sqrt{2^{p-1}(K-1)p!\sqrt{\pi}\sigma}} \exp\left(-\frac{x^2}{2\sigma^2}\right) H_p\left(\frac{x}{\sigma}\right) \tag{7.9}$$

and thus the Gaussian–Hermite moment of order p in the discrete case is given by

$$\eta_p = \sum_{i=0}^{K-1} \hat{H}_p(i, K; \sigma) I(i). \tag{7.10}$$

Finally, the inverse moment transformation can be carried out with its all moments of orders ($p \leq N_{max}$) by

$$\hat{I}(i) = \sum_{p=0}^{N_{max}} \eta_p \hat{H}_p(i, K; \sigma). \tag{7.11}$$

The extension to 2D, 3D even high–dimension spaces is straightforward. The only difference is the generation of counterparts of the basis functions. For example, in 2D space, the basis functions should be $\hat{H}_p(i, K; \sigma)\hat{H}_q(j, K; \sigma)$ for an image whose size

is $K \times K$ pixels. In 3D space, they should be $\hat{H}_p(i, K; \sigma)\hat{H}_q(j, K; \sigma)\hat{H}_r(k, K; \sigma)$ for an image in a $K \times K \times K$ voxels cube.

7.3 Rotation Invariants of Gaussian–Hermite Moments

Gaussian–Hermite polynomials belong to the family of functions orthogonal on a square in 2D and on a cube in 3D. Generally, it is difficult to derive rotation invariants from such moments because they transform themselves under rotation in a complicated manner. That is why most authors, when dealing with orthogonal moments, have preferred polynomial systems orthogonal on a unit disc, such as Zernike and Pseudo-Zernike polynomials, where the invariance can be easily achieved by a proper phase cancellation. However, working with these polynomials requires image mapping into the unit disc, which introduces resampling errors.

   In case of traditional geometric and complex moments, the rotation invariants are known and comprehensively studied [7]. In this section we derive rotation invariants from Gaussian–Hermite moments. We accomplish this using an interesting property of Hermite polynomials. We show that Gaussian–Hermite moments are transformed under rotation in exactly the same way as geometric moments. This property enables us to construct rotation invariants from Gaussian–Hermite moments in both 2D and 3D cases indirectly and very easily.

7.3.1 Rotation Invariants in 2D Case

7.3.1.1 Mathematical Preliminaries

We define non–coefficient Gaussian–Hermite moments as

$$\widetilde{\eta}_{pq} = \int_{-\infty}^{\infty} \int_{-\infty}^{\infty} \widetilde{H}_p(x; \sigma)\widetilde{H}_q(y; \sigma)f(x, y)dxdy, \tag{7.12}$$

with

$$\widetilde{H}_p(x; \sigma) = \sqrt{2^p p! \sqrt{\pi}\sigma}\hat{H}_p(x; \sigma). \tag{7.13}$$

In order to achieve translation invariance, we use central moments

$$\overline{\eta}_{pq} = \int_{-\infty}^{\infty} \int_{-\infty}^{\infty} \widetilde{H}_p(x - x_0; \sigma)\widetilde{H}_q(y - y_0; \sigma)f(x, y)dxdy, \tag{7.14}$$

where $x_0 = m_{10}/m_{00}$ and $y_0 = m_{01}/m_{00}$ are computed by the geometric moments

$$m_{pq} = \int_{-\infty}^{\infty} \int_{-\infty}^{\infty} x^p y^q f(x, y)dxdy, \tag{7.15}$$

In 2D space, there is only one parameter θ determining the rotation. Yang et al. discovered an important rotation property of Hermite polynomials [36].

Theorem 1. *Let p, q be two non–negative integers. Let the coordinates be rotated as*

$$\begin{pmatrix} \hat{x} \\ \hat{y} \end{pmatrix} = \begin{pmatrix} \cos\theta & -\sin\theta \\ \sin\theta & \cos\theta \end{pmatrix} \begin{pmatrix} x \\ y \end{pmatrix} \tag{7.16}$$

Then the following equation holds

$$\hat{x}^p \hat{y}^q = \sum_{r=0}^{p+q} k(r,p,q,\theta) x^{p+q-r} y^r, \tag{7.17}$$

where $k(r,p,q,\theta)$ is a coefficient which is determined by p, q, and θ. Moreover the product of Hermite polynomials can also be expressed as:

$$H_p(\hat{x}) H_q(\hat{y}) = \sum_{r=1}^{p+q} k(r,p,q,\theta) H_{p+q-r}(x) H_r(y). \tag{7.18}$$

The proof of Theorem 1 can be found in Appendix of [36].

Assume an original image $f(x,y)$ is rotated by angle θ. Here, we use f^θ to denote the rotated image. After rotation the original coordinates (x,y) are changed to $(\hat{x}, \hat{y})$. According to Eq.(7.12), non–coefficient Gaussian–Hermite moments of f^θ are therefore computed by

$$\widetilde{\eta}_{pq}^\theta = \int_{-\infty}^{\infty} \int_{-\infty}^{\infty} \widetilde{H}_p(\hat{x}; \sigma) \widetilde{H}_q(\hat{y}; \sigma) f^\theta(\hat{x}, \hat{y}) d\hat{x} d\hat{y}. \tag{7.19}$$

Rotation does not change image intensity function and the scaling of image, which means

$$\begin{cases} f^\theta(\hat{x}, \hat{y}) = f(x,y) \\ \quad d\hat{x} d\hat{y} = \det(\mathbf{R}) dx dy \end{cases}. \tag{7.20}$$

Matrix $\mathbf{R}$ is the transform matrix in Eq.(7.16). Using Theorem 1 and Eq.(7.20) as well, Eq.(7.19) is reduced into

$$\begin{aligned} \widetilde{\eta}_{pq}^\theta &= \int_{-\infty}^{\infty} \int_{-\infty}^{\infty} H_p\left(\frac{\hat{x}}{\sigma}\right) H_q\left(\frac{\hat{y}}{\sigma}\right) \exp\left(-\frac{x^2+y^2}{2\sigma^2}\right) f(x,y) dx dy \\ &= \sum_{r=0}^{p+q} k(r,p,q,\theta) \widetilde{\eta}_{p+q-r,r}. \end{aligned} \tag{7.21}$$

On the other hand, geometric moments also have similar relations before and after rotation

$$m_{pq}^\theta = \sum_{r=0}^{p+q} k(r,p,q,\theta) m_{p+q-r,r}. \tag{7.22}$$

In case of geometric moments, any rotation invariant can be expressed as a combination of certain set of moments χ which is capable of eliminating the angle θ. According to this fact, Eq.(7.21) and Eq.(7.22) altogether, we have an important conclusion related to the construction of rotation invariants from Gaussian–Hermite moments. We summarize the conclusion as the following theorem.

Theorem 2. *If χ is a rotation invariant in geometric moments*

$$\chi\left(m_{p_1q_1}^{\theta}, m_{p_2q_2}^{\theta}, \cdots, m_{p_iq_i}^{\theta}\right) = \chi\left(m_{p_1q_1}, m_{p_2q_2}, \cdots, m_{p_iq_i}\right). \tag{7.23}$$

then χ is also a rotation invariant in central non-coefficient Gaussian–Hermite moments, i.e.

$$\chi\left(\overline{\eta}_{p_1q_1}^{\theta}, \overline{\eta}_{p_2q_2}^{\theta}, \cdots, \overline{\eta}_{p_iq_i}^{\theta}\right) = \chi\left(\overline{\eta}_{p_1q_1}, \overline{\eta}_{p_2q_2}, \cdots, \overline{\eta}_{p_iq_i}\right). \tag{7.24}$$

In Theorem 2 the usage of the central moments $\overline{\eta}_{pq}$ enables the constructed invariant to possess translation invariance simultaneously. Theorem 2 means that we can use the formation of 2D rotation invariants from geometric moments to build the invariants from Gaussian–Hermite moments. The operation is very simple: just replacing geometric moments by the corresponding non–coefficient Gaussian–Hermite moments in the expressions of geometric rotation invariants.

7.3.1.2 Complete Set of Rotation Invariants in 2D Case

We are interested in generating a complete set of rotation invariants from Gaussian–Hermite moments in 2D case. This is straightforward because Flusser proposed a method, how to compute a complete and independent set of rotation invariants from complex moments [5]. Thanks to the above Theorems and a direct link between geometric and complex moments [5] we just follow that way and propose a design of a complete set of Gaussian–Hermite invariants. Firstly, we define the variable d_{pq}

$$d_{pq} = \sum_{k=0}^{p} \sum_{j=0}^{q} \binom{p}{k} \binom{q}{j} (-1)^{q-j} i^{p+q-k-j} \overline{\eta}_{k+j,p+q-k-j}. \tag{7.25}$$

Note that d_{pq} is intentionally defined such that it resembles the complex moment. Hence, d_{pq} works as a bridge between Gaussian–Hermite moments and the expressions of rotation invariants expressed by complex moments. We can also prove that d_{pq} has properties similar to complex moments:

$$d_{pq} = (d_{qp})^* \tag{7.26}$$

and

$$d_{pq}^{\theta} = e^{i(p-q)\theta} d_{pq}, \tag{7.27}$$

where "*" denotes conjugation. Hence, we construct the rotation invariants according to [5] as

$$\Psi_{pq}(p_0, q_0) \equiv d_{pq} d_{q_0 p_0}^{p-q}, \text{ with } p \geq q, \ p_0 - q_0 = 1. \tag{7.28}$$

The indices p_0, q_0 should be chosen as low as possible to obtain good numerical stability. In the experiments in this paper we set $p_0 = 2, q_0 = 1$.
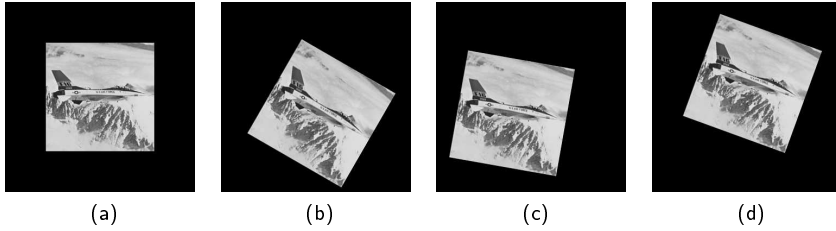
Figure 7.2: The images of F–16 fighter of the size 350×350 pixels used in the experiment. (a) The original images. (b)-(d) transformed images.

7.3.1.3 Invariance Verification

In this section we test the proposed 2D invariants on both synthesized and real rotations. Firstly, we verify rotation invariance of the invariants Eq.(7.28) under computer-generated rotations. An image of "F–16" fighter is used as the test image. We generate 7 random rotations and translations. Figure 7.2 shows the original image and 3 examples of the transformed versions. We compute 6 invariants in vector $\mathbf{V}$ for these test images.

$$\mathbf{V} = \Big[\mathrm{Re}(d_{4,3}d_{1,2}),\ \mathrm{Im}(d_{5,3}d_{1,2}^2),\ d_{6,7}d_{7,6},\ \mathrm{Re}(d_{8,7}d_{1,2}),\ d_{10,10},\ \mathrm{Im}(d_{11,10}d_{1,2})\Big].$$
$$(7.29)$$

The elements of $\mathbf{V}$ were selected in such a way that they contain invariants of various orders. Since the rotation model is perfectly valid, the computed invariants are expected to keep exact invariance even for the invariants of high orders (up to order 21 in this experiment). We set $\sigma = 0.3$. The values of the selected invariants are plotted in Fig.(7.3). It should be noted that we plot the scaled values (throwing away the orders of magnitude of the computed invariants) instead of their real values. For instance, V_1 computed from the original image is equal to -1.8292×10^5, while we plot -1.8292 instead. It enables to plot these 6 invariants in the same range of values. As can be seen from Fig.(7.3), for each invariant the values computed from the different images are kept almost constant. Consequently, the plots appear to be straight lines. In order to directly demonstrate the invariance, we use Mean Relative Error (MRE) to measure the computational error of the i-th invariant in $\mathbf{V}$. The MRE of the ith invariant is defined as

$$\mathrm{MRE}_i = \frac{1}{N}\sum_{j=1}^{N}\left|\frac{V_i^j - V_i}{V_i}\right| \times 100\%,\qquad(7.30)$$

where V_i and V_i^j are the i-th invariants computed from the original image and the j-th rotated version, respectively. N was the number of rotated versions. All MREs (caused mainly by resampling errors) are below 2.0% (see the caption of Fig.(7.3)).

The second experiment works not only with real images of a large size but also with real physical rotations. In this experiment we generate 8 images by scanning a hotel notice card in various orientations. The scanner does not change the scale of the card and it also produces almost the same illuminations of each scan. We segment the
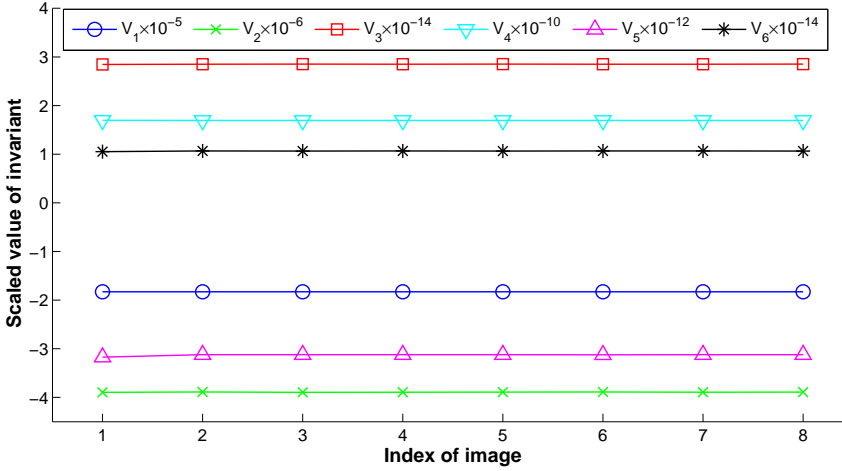
Figure 7.3: The values of the selected invariants computed from the F–16 images. Index 1 indicates the original image. The MREs of the invariants over 7 transformed versions are respectively 0.02%, 0.09%, 0.26%, 0.15%, 1.55% and 1.36%, respectively.

scanned images and put each into a square whose size is 1000×1000 pixels. Figure 7.4 displays the scanned images that we use in this experiment. We compute several Gaussian–Hermite invariants for these images. These invariants are elements of vector $\mathbf{W}$

$$\mathbf{W} = \Big[\mathrm{Im}(d_{5,4}d_{1,2}),\ d_{6,7}d_{7,6},\ \mathrm{Re}(d_{8,7}d_{1,2}),\ \mathrm{Re}(d_{9,8}d_{1,2}),\ d_{10,10},\ d_{12,12}\Big]. \quad (7.31)$$

We intentionally include different invariants from those in the previous experiment. This time we cannot calculate relative error because there is no "original" image. We use the ratio between the standard deviation of each invariants σ_v and its average μ_v to measure the error of each invariant. Figure 7.5 shows the values of the invariants. As can be seen from the figure, there are more visible changes in the values of invariants than those in Fig.(7.3). However, the changes are acceptable since all the errors are below 4.0%, which demonstrates the rotation invariance of the invariants and also shows their capability of working with real images.

7.3.2 Rotation Invariants in 3D Case

7.3.2.1 Mathematical Preliminaries

To describe 3D rotation mathematically, several conventions can be used. Two most widely applied conventions are Euler angle convention and Tait–Bryan angle convention [30]. They differ from each other in such a way that the Tait–Bryan convention always uses three angles around x, y, z axes while Euler convention may use the same axis twice. In other words, the Euler convention has one repeated axis in its definition while
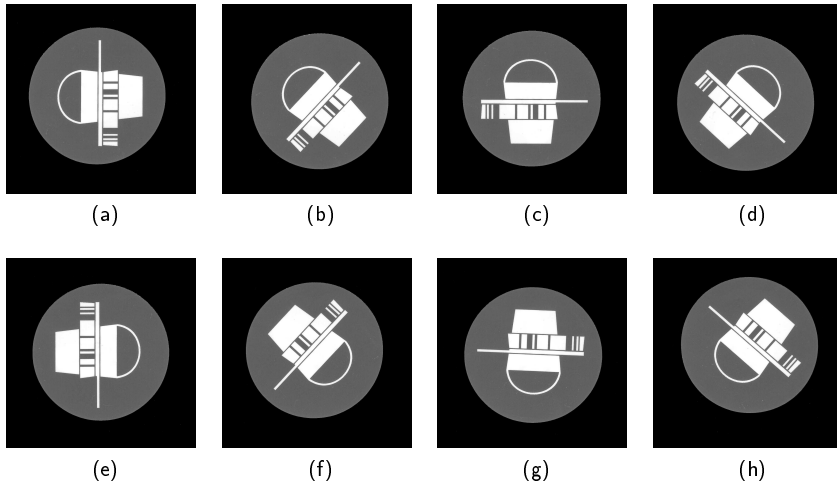
Figure 7.4: The scans of a notice card whose sizes are 1000×1000 pixels.
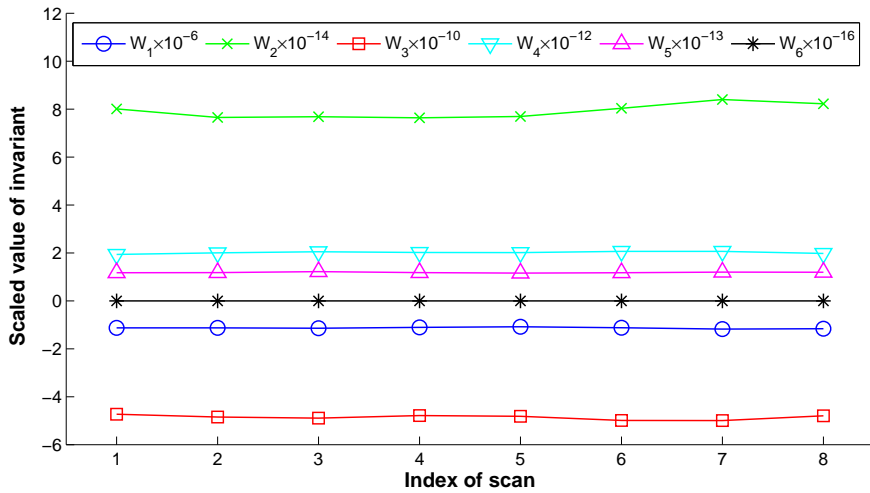
Figure 7.5: The values of the selected invariants computed from the scanned notice cards. The errors of the invariants over 8 transformed versions are 2.56%, 3.70%, 1.97%, 2.22%, 1.60% and 2.85%, respectively.

the Tait–Bryan convention always describes the rotation with the different axes. In spite of this, there are "intrinsic" rotation and "extrinsic" rotation for both Euler angle and Tait–Bryan angle conventions. Suppose that the reference coordinate system is denoted as (x, y, z); correspondingly, the mobile coordinate system is denoted as (X, Y, Z). "Intrinsic" rotation means that all rotations are performed along the moving axes. For example, an "intrinsic" rotation described by Euler angles is carried out with moving axes $(Z - X' - Z'')$. Comparatively, "extrinsic" rotation is implemented by rotating along the static axes $(z - y - x)$. Both Euler angle and Tait–Bryan angle conventions can be used to describe 3D rotation. For convenience, we use "extrinsic" Tait–Bryan angle convention $(z - y - x)$ in this Chapter. More specifically, we discuss the rotation which rotates firstly along z axis by angle α. The rotation matrix is,

$$\mathbf{R_z}(\alpha) = \begin{pmatrix} \cos\alpha & -\sin\alpha & 0 \\ \sin\alpha & \cos\alpha & 0 \\ 0 & 0 & 1 \end{pmatrix}. \tag{7.32}$$

Consequently, a rotation along y axis by angle $-\beta$ has the rotation matrix as follows,

$$\mathbf{R_y}(-\beta) = \begin{pmatrix} \cos\beta & 0 & \sin\beta \\ 0 & 1 & 0 \\ -\sin\beta & 0 & \cos\beta \end{pmatrix}. \tag{7.33}$$

Finally, a rotation along x axis by angle γ is formulated by,

$$\mathbf{R_x}(\gamma) = \begin{pmatrix} 1 & 0 & 0 \\ 0 & \cos\gamma & -\sin\gamma \\ 0 & \sin\gamma & \cos\gamma \end{pmatrix}. \tag{7.34}$$

So, such a 3D rotation can be directly represented by a matrix multiplication,

$$\mathbf{R} = \mathbf{R_x}(\gamma)\mathbf{R_y}(-\beta)\mathbf{R_z}(\alpha). \tag{7.35}$$

Any rotation in 3D space can be decomposed into three successive rotations as defined by Eq.(7.35). In other words, the rotation $(z - y - x)$ by $(\alpha, -\beta, \gamma)$ can accomplish an arbitrary rotation in 3D space. So, we only discuss this specific case. The conclusion is also valid for other rotation conventions.

7.3.2.2 Constructing Rotation Invariants

Theorem 1 offers an opportunity of studying the behavior of Hermite polynomials under 3D rotation, because a 3D rotation is actually composed of three successive rotations in 2D. We have proved that when 3D rotation occurs, Hermite polynomials behave similarly to monomials. The following Theorem formulates this conclusion more formally.

Theorem 3. *Let p, q, and r be non-negative integers. Let the coordinates be rotated as*

$$(\hat{x}\ \hat{y}\ \hat{z})^T = \mathbf{R}\,(x\ y\ z)^T, \tag{7.36}$$

where T is a matrix transposition. Then

$$\hat{x}^p \hat{y}^q \hat{z}^r = \sum_{i=1}^{L(p,q,r)} con_i\,(p,q,r,\alpha,\beta,\gamma)\, x^{p_i} y^{q_i} z^{r_i}, \qquad (7.37)$$

where $L(p,q,r)$ is a certain number determined by p,q,r. The con_i represents a constant sequence specifically related to p,q,r,α,β and γ. The p_i, q_i, r_i are integers determined by p,q,r. Hermite polynomials are transformed in the same way, i.e. it holds

$$H_p(\hat{x})H_q(\hat{y})H_r(\hat{z}) = \sum_{i=1}^{L(p,q,r)} con_i\,(p,q,r,\alpha,\beta,\gamma)\, H_{p_i}(x)H_{q_i}(y)H_{r_i}(z). \qquad (7.38)$$

The proof of Theorem 3 can be found in Appendix A of [35]. It is easy to prove that with the same standard deviations $\sigma_x = \sigma_y = \sigma_z$, a 3D Gaussian function is rotation invariant. So, multiplying both sides of Eq.(7.38) by a 3D Gaussian function does not violate the equality. Finally, we can draw the central conclusion that rotation invariants of Gaussian-Hermite moments have the same constructing formations as those of rotation invariants of geometric moments in 3D space, which is formally expressed in the following Theorem.

Theorem 4. If χ is a rotation invariant in geometric moments

$$\chi\left(m_{p_1q_1r_1}^{\alpha\beta\gamma}, m_{p_2q_2r_2}^{\alpha\beta\gamma}, \cdots, m_{p_iq_ir_i}^{\alpha\beta\gamma}\right) = \chi\left(m_{p_1q_1r_1}, m_{p_2q_2r_2}, \cdots, m_{p_iq_ir_i}\right) \qquad (7.39)$$

then χ is also a rotation invariant in Gaussian–Hermite moments, i.e.

$$\chi\left(\overline{\eta}_{p_1q_1r_1}^{\alpha\beta\gamma}, \overline{\eta}_{p_2q_2r_2}^{\alpha\beta\gamma}, \cdots, \overline{\eta}_{p_iq_ir_i}^{\alpha\beta\gamma}\right) = \chi\left(\overline{\eta}_{p_1q_1r_1}, \overline{\eta}_{p_2q_2r_2}, \cdots, \overline{\eta}_{p_iq_ir_i}\right), \qquad (7.40)$$

where $\overline{\eta}_{pqr}$ is a non-coefficient central 3D Gaussian–Hermite moment

$$\overline{\eta}_{pqr} = \int_{-\infty}^{\infty}\int_{-\infty}^{\infty}\int_{-\infty}^{\infty} \widetilde{H}_p(x-x_c;\sigma)\widetilde{H}_q(y-y_c;\sigma)\widetilde{H}_r(z-z_c;\sigma)f(x,y,z)dxdydz. \qquad (7.41)$$

The centroid of the image $f(x,y,z)$ is calculated by $x_c = m_{100}/m_{000}$, $y_c = m_{010}/m_{000}$ and $z_c = m_{001}/m_{000}$. The proof of Theorem 4 is given in Appendix B of [35].

Rotation invariant construction based on Gaussian–Hermite moments becomes convenient in 3D space as well. If we find a rotation invariant of geometric moments and then replace the geometric moments by the corresponding Gaussian–Hermite moments, we obtain a rotation invariant from Gaussian–Hermite moments.

Recently, Suk and Flusser proposed and implemented an automatic method for generating 3D rotation invariants from geometric moments. Their complete results are summarized in [27]. A list of 1185 irreducible rotation invariants in 3D space is available there. These invariants are built up from the moments of order 2 up to order 16. For example,

$$I_1 = \mu_{200} + \mu_{020} + \mu_{002}, \qquad (7.42)$$

$$I_2 = \mu_{200}^2 + \mu_{020}^2 + \mu_{002}^2 + 2\mu_{110}^2 + 2\mu_{101}^2 + 2\mu_{011}^2, \qquad (7.43)$$

$$I_3 = \mu_{200}^3 + 3\mu_{200}\mu_{110}^2 + 3\mu_{200}\mu_{101}^2 + 3\mu_{110}^2\mu_{020}$$
$$+ 3\mu_{101}^2\mu_{002} + \mu_{020}^3 + 3\mu_{020}\mu_{011}^2 + 3\mu_{011}^2\mu_{002} \qquad (7.44)$$
$$+ \mu_{002}^3 + 6\mu_{110}\mu_{101}\mu_{011},$$

$$I_4 = \mu_{300}^2 + \mu_{030}^2 + \mu_{003}^2 + 3\mu_{210}^2 + 3\mu_{201}^2$$
$$+ 3\mu_{120}^2 + 3\mu_{102}^2 + 3\mu_{021}^2 + 3\mu_{012}^2 + 6\mu_{111}^2, \qquad (7.45)$$

$$I_5 = \mu_{300}^2 + 2\mu_{300}\mu_{120} + 2\mu_{300}\mu_{102} + 2\mu_{210}\mu_{030}$$
$$+ 2\mu_{201}\mu_{003} + \mu_{030}^2 + 2\mu_{030}\mu_{012} + 2\mu_{021}\mu_{003}$$
$$+ \mu_{003}^2 + \mu_{210}^2 + 2\mu_{210}\mu_{012} + \mu_{201}^2 + 2\mu_{201}\mu_{021} \qquad (7.46)$$
$$+ \mu_{120}^2 + 2\mu_{120}\mu_{102} + \mu_{102}^2 + \mu_{021}^2 + \mu_{012}^2$$

are the first five rotation invariants. According to Theorem 4, we replace every geometric moment by the corresponding Gaussian–Hermite moment in these invariants and then we obtain rotation invariants of Gaussian–Hermite moments. For example, the first rotation invariant from Gaussian–Hermite moments is

$$\Phi_1 = \overline{\eta}_{200} + \overline{\eta}_{020} + \overline{\eta}_{002}. \qquad (7.47)$$

It is possible to use all invariants presented in [27] to build the invariants of Gaussian–Hermite moments. Following this way, we can easily obtain totally 1185 rotation invariants of orthogonal Gaussian–Hermite moments.

7.3.2.3 Invariance Verification

As in the 2D case, we verify rotation invariance in 3D space via both synthesized and real images. A shape showing a dog is selected from Princeton Shape Benchmark (PSB) [22]. We rasterized this mesh model and inscribed it into $200 \times 200 \times 200$ volume, which is illustrated as the original image in Fig.(7.6a). This original image only had two values to its voxels: 1 for the object voxels and 0 for those of the background. Ten random rotations of the original image are generated (see Fig.(7.6b)) and Gaussian–Hermite invariants Φ_4, Φ_{43}, Φ_{243}, Φ_{584}, Φ_{841} and Φ_{1012} are calculated for original image and all its rotated versions. These invariants are respectively constructed from the moments of different orders (from order 3 to 8). So they represent the invariants of different orders. The parameter $\sigma = 0.3$ is set for invariant computation.

The results are illustrated in Fig.(7.7), from which we can observe that each selected invariant almost has unchanged values. The corresponding plotting looks like a line. Moreover, MREs (replacing V_i by Φ_i in Eq.(7.30)) are also quite tiny and they are far below 1.0% absolutely. So, rotation invariance is well confirmed.

We carry out a similar experiment with the real images – real 3D object and its real rotations in the space. We use a teddy bear and scan it by means of Kinect device, then we repeat this process five times with different orientations of the teddy bear in the space. Hence, we obtain six 3D scans differing from each other by rotation and also slightly by scale, quality of details and perhaps by some random errors. Figure 7.8 illustrates two samples of the scanned bear. The generating of the scanned image is as follows. Firstly, it needs scan the bear from several views and Kinect software then

(a) Original image   (b) Rotated image
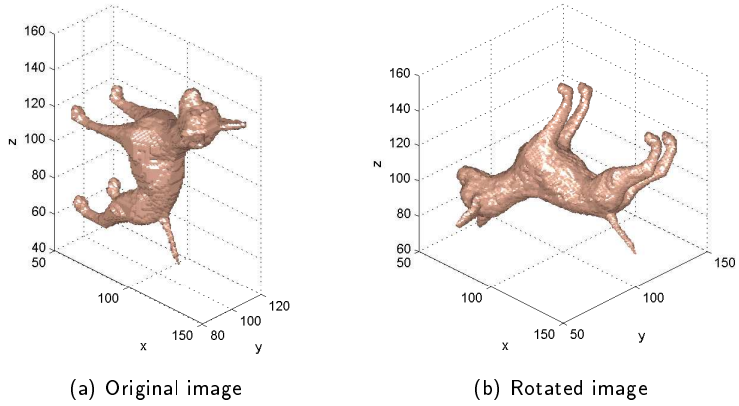
Figure 7.6: The "Dog" from Princeton Shape Benchmark (PSB).
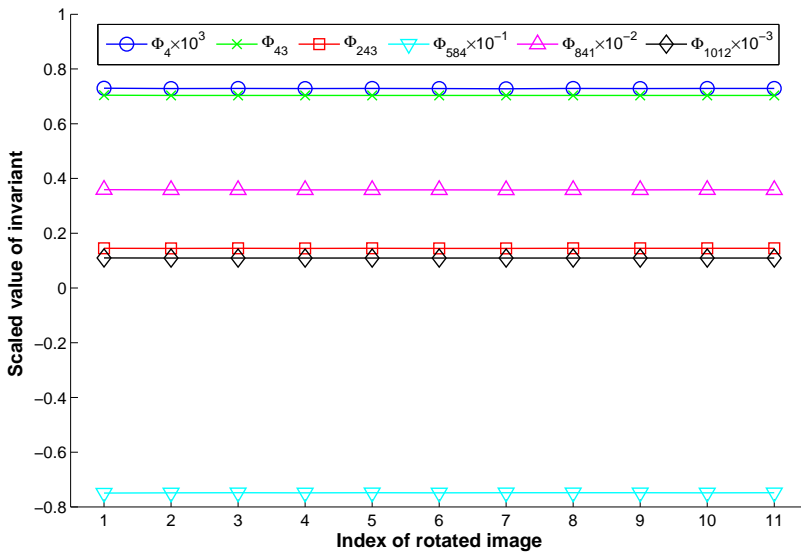
Figure 7.7: The values of six selected invariants of the "Dog". Index 1 indicates the original image. The errors of the invariants over ten rotations are 0.15%, 0.10%, 0.21%, 0.14%, 0.28%, and 0.18% respectively.

(a) The first scan   (b) The second scan
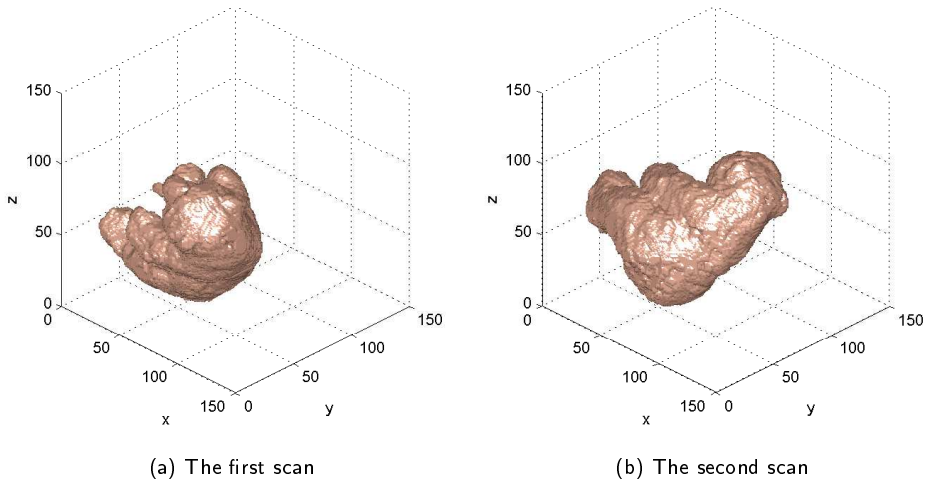
Figure 7.8: Two scans of a teddy bear.

produces a triangulated surface of the object automatically. Secondly, we convert each teddy bear figure into 3D volumetric representation of the size approximately $150 \times 150 \times 150$ voxels. We calculate the first 21 invariants Φ_1 to Φ_{21} of each scan, with the choice of $\sigma = 0.3$. For measuring the stability of the invariance, we also use $|\sigma_v/\mu_v|\%$ of each invariant. In Fig.(7.9) we show 6 randomly selected invariants computed from the different scans. Note that we plot the scaled values of the invariants again for display reason. As can be seen from this figure, the values of the invariants have only slight variances; For invariants Φ_8 and Φ_{21} their variances are relatively greater. The plots look like fold lines. The errors show the details information about the variances. However, the errors are in reasonably low degree (below 5.0%). So, they all confirm the desirable invariance of the proposed invariants in a real environment.

7.4 Image Reconstruction from Gaussian–Hermite Moments

Image reconstruction is in fact an inverse moment transform and illustrates the discrimination power of the (complete or partial) set of moments. An obvious advantage of orthogonal moments is their efficiency in image reconstruction. This efficiency is brought by the orthogonality of their basis functions. Generally, it is easy to reconstruct an image from its orthogonal moments. For orthogonal basis functions $\psi_{pq}(x, y)$, image reconstruction from the orthogonal moments M_{pq} is computed as

$$f(x, y) = \sum_{p=0}^{N_{max}} \sum_{q=0}^{N_{max}} M_{pq} \psi_{pq}(x, y) \tag{7.48}$$
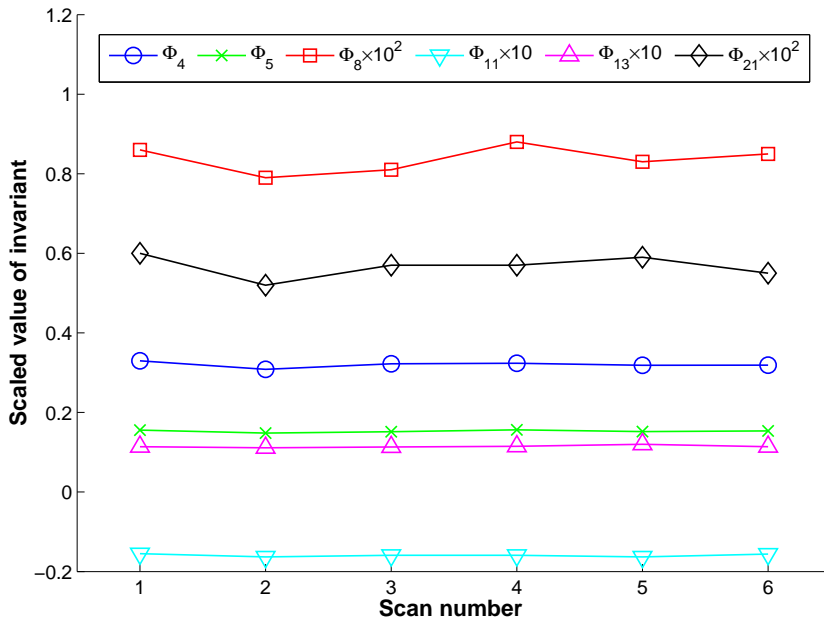
Figure 7.9: The values of six selected invariants of the teddy bear. The errors of the invariants over six rotations are 2.21%, 1.92%, 3.80%, 2.22%, 2.55%, and 4.90% respectively.

(an analogous relation holds in any dimension). This reconstruction is "optimal" because it minimizes the mean square error when using only a finite set of moments. On the other hand, image reconstruction from geometric moments cannot be performed directly in the spatial domain. It is carried out in the Fourier domain using the fact that geometric moments form Taylor coefficients of the Fourier transform $F(u, v)$

$$F(u, v) = \sum_{p=0}^{\infty} \sum_{q=0}^{\infty} \frac{(-2\pi i)^{p+q}}{p! q!} u^p v^q m_{pq}. \tag{7.49}$$

Reconstruction of $f(x, y)$ is then achieved via inverse Fourier transform [7]. In this Section, we first recall 2D image reconstruction using Gaussian–Hermite moments as it was originally presented in [34, 33] and then we extend the reconstruction also to a 3D case.

7.4.1 Image Reconstruction in 2D Case

7.4.1.1 Parameter Selection

Image reconstruction from Gaussian–Hermite moments in 2D space is described by

$$\hat{I}(i, j) = \sum_{p=0}^{N_{max}} \sum_{q=0}^{N_{max}} \eta_{pq} \hat{H}_p(i, K; \sigma) \hat{H}_q(j, K; \sigma). \tag{7.50}$$

There is a scale parameter σ in the basis functions of Gaussian–Hermite moments which influences the quality of the reconstruction. Given the same moments for image reconstruction, greater σ produces a larger reconstructed area but a relatively poor accuracy while less σ results in a smaller reconstructed area, however with better accuracy. We demonstrate this via reconstructing an image "baboon" whose size is 128×128 pixels (see Fig.(7.10a)). The reconstructed images from the same set of moments are given in Fig.(7.10b) and Fig.(7.10c). Apparently, the reconstructed images are quite different if we use different σ.

(a)   (b)   (c)   (d)
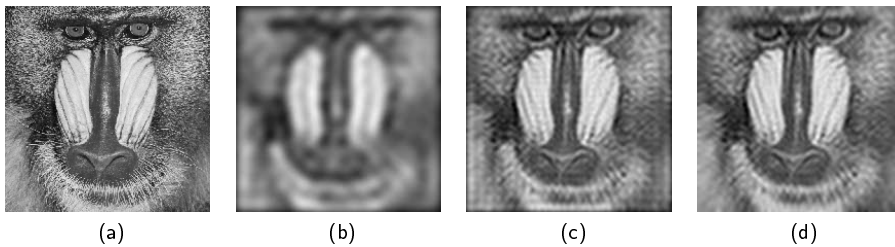
Figure 7.10: Images reconstructed from Gaussian–Hermite moments. (a) The original gray–level image "baboon" of size 128×128 pixels. (b) The reconstructed image from the moments of orders $(0, 0)$ up to $(49, 49)$ with $\sigma = 0.30$. (c) The reconstructed image from the same moments as (b) with $\sigma = 0.1189$. (d) The reconstructed image (c) followed by the normalization.

Therefore, σ should be selected carefully. We should make a compromise, which balances the size of the reconstruction area and the accuracy. The role of the σ is to suppress the boundary part of the image which is prone to reconstruction errors.

It is difficult or even impossible to find any "theoretically optimal" σ. It is a function of the image size $K \times K$ and of the order N_{max} of the moments used in the reconstruction. We solved this experimentally for the complete reconstruction, i.e. $N_{max} = K - 1$. Provided that σ is a power function of N_{max}, we discovered an empirical relation

$$\sigma = 0.9 \times N_{max}^{-0.52}. \tag{7.51}$$

In the sequel, we use this choice of σ. For example, Fig.(7.10c) is calculated with such σ and we can observe that the reconstruction is relatively good, particularly in comparison with Fig. 7.10(b) where higher σ was used.

There are some defects appearing as horizontal and vertical textures around the border of image in Fig.(7.10c). We suggest a normalization operation to get rid of these textures. The normalization operation is described mathematically by

$$\tilde{I}(i,j) = \frac{\hat{I}(i,j)}{\sum_{p=0}^{N_{max}} \sum_{q=0}^{N_{max}} \mu_{pq} \hat{H}_p(i, K; \sigma_N) \hat{H}_q(j, K; \sigma_N)}, \tag{7.52}$$

where

$$\mu_{pq} = \sum_{i=0}^{K-1} \sum_{j=0}^{K-1} \hat{H}_p(i, K; \sigma_N) \hat{H}_q(j, K; \sigma_N). \tag{7.53}$$

$\hat{I}(i,j)$ and $\tilde{I}(i,j)$ denote respectively the reconstructed image from Eq.(7.50) and the final reconstructed image after normalization operation. Figure 7.10d shows the effect of normalization operation. Compared with Fig.(7.10c), the textures around the border have disappeared.

7.4.1.2 Reconstruction of a Binary Image

An example of reconstructing a binary image is given in this section. A binary image showing a scorpion serves as the test image. This image has a size 96×96 pixels. We compare the reconstruction power of Gaussian–Hermite moments with the most popular other moments such as exact Legendre [11], discrete Tchebichef [20] and Krawtchouk [37] moments. The measure of the reconstruction quality is the number of different pixels between the original image and the reconstructed image:

$$e = \sum_{i=0}^{K-1} \sum_{j=0}^{K-1} \left| I(i,j) - T(\hat{I}(i,j)) \right|, \tag{7.54}$$

where $T(z)$ is the threshold operator:

$$T(z) = \begin{cases} 1 & z \geq 0.5 \\ 0 & z < 0.5 \end{cases} \tag{7.55}$$
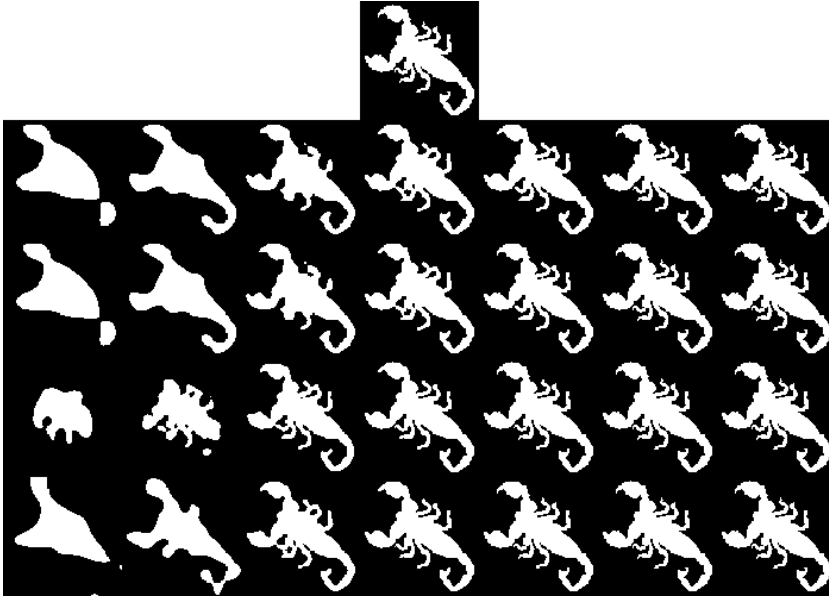
Figure 7.11: Binary image reconstruction of the image "scorpion" whose size is 96×96 pixels. From left to right, the maximum moment indices are $(6,6)$, $(12,12)$, $(27,27)$, $(42,42)$, $(57,57)$, $(72,72)$, and $(90,90)$. From the top to bottom, each row shows the reconstructions from exact Legendre, discrete Tchebichef, Krawtchouk and Gaussian–Hermite moments, respectively.

The reconstructed images are displayed in Fig.(7.11) with the corresponding reconstruction errors recorded in Table 7.1. As can be seen from Fig.(7.11), Gaussian–Hermite moments produce better reconstruction than the other moments on the whole. This can be demonstrated visually by the separated claws, however some methods create the claws which are connected to be a mass. For each maximum order of the reconstruction, the reconstruction error corresponding to Gaussian–Hermite moments is almost the lowest one among all tested methods. This indicates the best performance in image representation ability of Gaussian–Hermite moments when the reconstruction of a binary image is required.

7.4.1.3 Reconstruction of a Gray–Level Image

A gray–level image "Lena" whose size is 100×100 is used as the test image for reconstruction. As a measure of the reconstruction quality, we adopt Peak Signal-to-Noise Ratio (PSNR). The PSNR value is defined by

$$\text{PSNR} = 10\log_{10}\frac{255^2}{\text{MSE}}, \tag{7.56}$$

Table 7.1: Reconstruction error of the image "scorpion".

Order n	6	12	27	42	57	72	90
Exact Legendre e	1058	727	377	176	78	23	7
Discrete Tchebichef e	1057	727	358	159	55	9	0
Krawtchouk e	1366	1012	191	63	20	1	0
Gaussian–Hermite e	1109	711	215	62	11	0	0

with MSE denoting the Mean Square Error of the reconstructed image with respect to the original image:

$$\text{MSE} = \frac{1}{K^2} \sum_{i=0}^{K-1} \sum_{j=0}^{K-1} \left(I(i,j) - \hat{I}(i,j) \right)^2. \tag{7.57}$$

Several selected reconstructed images are shown in Fig.(7.12). The more detailed information about the PSNR is depicted in Fig.(7.13). As can be seen in Fig.(7.12), Gaussian–Hermite moments produce the best reconstruction among these four methods. The detailed information, such as the area around Lena's eyes, are clearly displayed in the reconstruction from Gaussian–Hermite moments. Exact Legendre and discrete Tchebichef however give corrupted reconstruction around the eyes. This is confirmed by the reconstruction with the maximum orders equal to 14 and 41 respectively. The plot of PSNR also shows that Gaussian–Hermite moments yield the highest PSNR at most orders and very close to the highest at the other orders. It should be however noted that the differences in PSNR are not big.

7.4.2 Image Reconstruction in 3D Case

Image reconstruction in 3D case is straightforward with Gaussian–Hermite moments. The only difference is that both the image and the basis functions are three-dimensional.

Assuming that $f(x,y,z)$ is a volumetric image, its Gaussian–Hermite moments are computed by Eq.(7.7). Image reconstruction therefore has the form

$$\hat{I}(i,j,k) = \sum_{p=0}^{N_{max}} \sum_{q=0}^{N_{max}} \sum_{r=0}^{N_{max}} \eta_{pqr} \hat{H}_p(i,K;\sigma_N) \hat{H}_q(j,K;\sigma_N) \hat{H}_r(k,K;\sigma_N). \tag{7.58}$$

When reconstructing image with Eq.(7.58), σ selection should also be executed by Eq.(7.51). Equation 7.52 on the other hand should be updated to

$$\tilde{I}(i,j,k) = \frac{\hat{I}(i,j,k)}{\sum_{p=0}^{N_{max}} \sum_{q=0}^{N_{max}} \sum_{r=0}^{N_{max}} \mu_{pqr} \hat{H}_p(i,K;\sigma_N) \hat{H}_q(j,K;\sigma_N) \hat{H}_r(k,K;\sigma_N)}, \tag{7.59}$$

where

$$\mu_{pqr} = \sum_{i=0}^{K-1} \sum_{j=0}^{K-1} \sum_{k=0}^{K-1} \hat{H}_p(i,K;\sigma_N) \hat{H}_q(j,K;\sigma_N) \hat{H}_r(k,K;\sigma_N). \tag{7.60}$$

Figure 7.12: Image reconstruction of the gray-level image "Lena" of size 100×100 pixels. From left to right, the maximum indices of the moments are $(14, 14)$, $(41, 41)$, $(68, 68)$ and $(95, 95)$. From top to the bottom, the exact Legendre, discrete Tchebichef, Krawtchouk and Gaussian–Hermite moments were used.
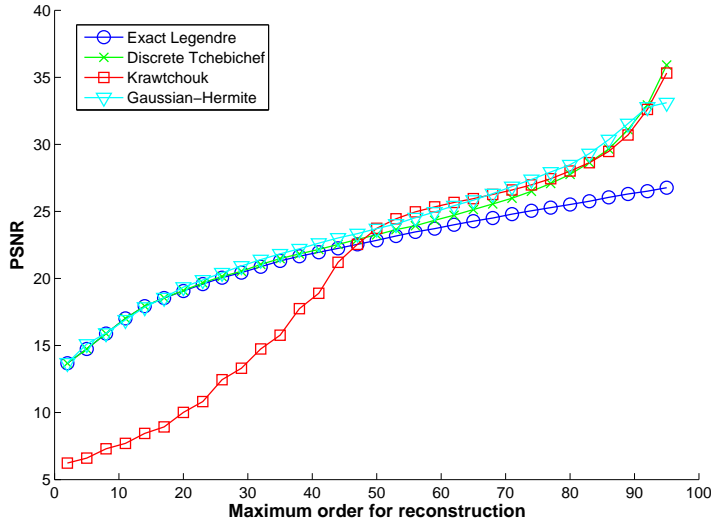
Figure 7.13: Comparative study of reconstruction error of exact Legendre, discrete Tchebichef, Krawtchouk and Gaussian–Hermite moments of the image "Lena".

However, since moment computation from volumetric images is time–consuming, the reconstruction becomes even more tendentiously longer, especially for large images. So, we conduct 3D image reconstruction only with small images in general.

For comparison purpose, we also consider image reconstruction from geometric moments in 3D case. We adopt the algorithm based on Fourier transform. In 3D space, we are able to realize image reconstruct by the following formula

$$F(u, v, w) = \sum_{p=0}^{\infty} \sum_{q=0}^{\infty} \sum_{r=0}^{\infty} \frac{(-2\pi i)^{p+q+r}}{p!q!r!} \left(\frac{u}{K}\right)^p \left(\frac{v}{K}\right)^q \left(\frac{w}{K}\right)^r m_{pqr}. \qquad (7.61)$$

Subsequently, an inverse Fourier transform will generate the reconstructed image. Discrete Tchebichef and Krawtchouk moments are also extended to 3D space and applied to image reconstruction for comparison. We give an example of 3D image reconstruction. A mesh model showing a spider is selected from the PSB. We transform the mesh model into voxels and inscribe it into $100 \times 100 \times 100$ volume, see Fig.(7.14a). This volumetric image is binary and has only two values in its voxels: 0 for the background and 1 for the object.

We reconstruct this image with the different maximum orders (see figures from Fig.(7.14b) to (k)). In order to specify the quality of the reconstructed images, the number of different voxels between the original image and the reconstructed image is taken as the error measure. As can be seen from Fig.(7.14), the reconstructed images have ever–increasing quality with the maximum order increasing. We can observe Fig.(7.14c), (7.14f) and (7.14i) that only the body and the head of the spider are re-

constructed with lower orders. With the maximum order increasing, Gaussian–Hermite and Krawtchouk moments reconstruct vividly the legs; however, discrete Tchebichef moments fail to reconstruct these parts. When the maximum order reaches to 84, Gaussian–Hermite moments can completely reconstruct the original image (with error 0), which exhibits the best performance in comparison with Krawtchouk moments (with error only 17) and discrete Tchebichef moments (with error 98). The maximum achievable order of geometric moment is 84 for the image "Spider". The computation of moments whose order is greater than 84 will result in numerical overflow. However, even if we use the moments up to the maximum achievable order, the reconstruction is still of a poor, insufficient quality (see Fig.(7.14b)). As a result, this experiment shows that in the 3D case, Gaussian–Hermite moments have better image representation ability than geometric moments and some orthogonal moments such as discrete Tchebichef and Krawtchouk moments.

7.5 Application of Gaussian–Hermite Invariants in Image Registration

In this Section, we demonstrate the application of Gaussian–Hermite invariants (GHIs) in template matching as well as in image registration. The experiment is carried out on an aerial image in Fig.(7.15a) which was downloaded from [21]. We rotated this image by $30°$ clockwise and then shifted it horizontally and vertically by 30 and 40 pixels, respectively. The rotated image served as our reference image. We detected 100 most prominent corners, road junctions and other significant points which we took as the control point candidates (CPC). Around each CPC we took a circular template of a diameter 51 pixels, see Fig.(7.16).

To simulate real image degradations, we blurred the original image by a simulated atmospheric turbulence blur and then a Gaussian white noise was added. We created two instances with mild and heavy noise, see Fig.(7.15b) and (7.15c). These images played the role of sensed images (i.e. images to be registered).

Our goal is to locate these 100 templates in two degraded sensed images. The template matching is carried out by two methods: Geometric invariants (GEIs) and GHIs. The feature vector is composed of 18 invariants up to the order 5. According to [5], the feature vector corresponding to GEIs is

$$
\begin{aligned}
\mathbf{V}_g = \Big[& c_{11},\ c_{21}c_{12},\ \mathrm{Re}(c_{20}c_{12}^2),\ \mathrm{Im}(c_{20}c_{12}^2),\ \mathrm{Re}(c_{30}c_{12}^3),\ \mathrm{Im}(c_{30}c_{12}^3),\ c_{22}, \\
& \mathrm{Re}(c_{31}c_{12}^2),\ \mathrm{Im}(c_{31}c_{12}^2),\ \mathrm{Re}(c_{40}c_{12}^4),\ \mathrm{Im}(c_{40}c_{12}^4),\ c_{32}c_{23},\ \mathrm{Re}(c_{32}c_{12}), \\
& \mathrm{Im}(c_{32}c_{12}),\ \mathrm{Re}(c_{41}c_{12}^3),\ \mathrm{Im}(c_{41}c_{12}^3),\ \mathrm{Re}(c_{50}c_{12}^5),\ \mathrm{Im}(c_{50}c_{12}^5) \Big],
\end{aligned}
$$

$$
\tag{7.62}
$$

(a) Original image   (b) Order 84 error 8561

(c) Order 26 error 1333   (d) Order 46 error 1003   (e) Order 84 error 98

(f) Order 26 error 955   (g) Order 46 error 435   (h) Order 84 error 17

(i) Order 26 error 1054   (j) Order 46 error 370   (k) Order 84 error 0
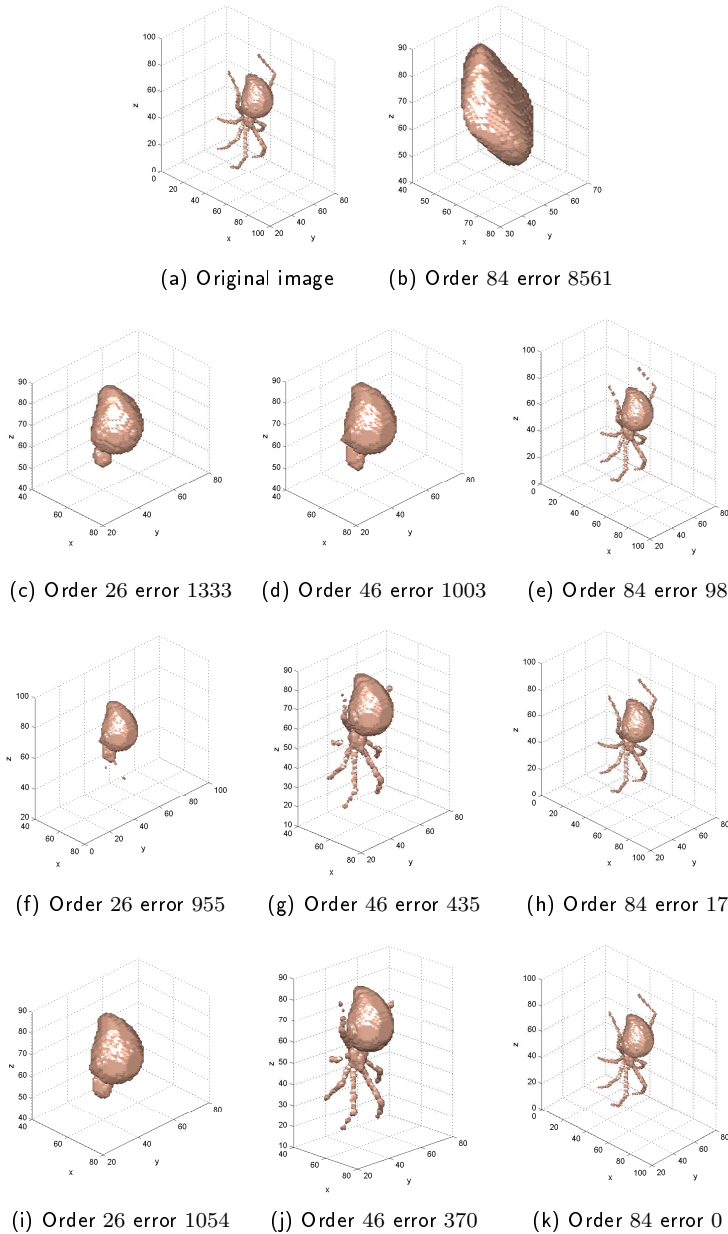
Figure 7.14: The reconstruction of a volumetric image by different kinds of moments. (a) The original image whose size is $100 \times 100 \times 100$ voxels; the reconstructed images by (b) geometric moments of orders $(0,0,0)$ up to $(84,84,84)$, (c) (d) and (e) by discrete Tchebichef moments, (f) (g) and (h) by Krawtchouk moments. (i) (j) and (k) by Gaussian–Hermite moments.

(a)   (b)   (c)
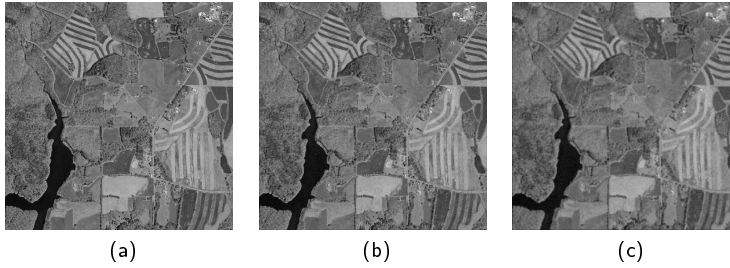
Figure 7.15: The images used in the experiment. (a) The original aerial image. (b) The degraded image with mild noise. (c) The degraded image with heavy noise.
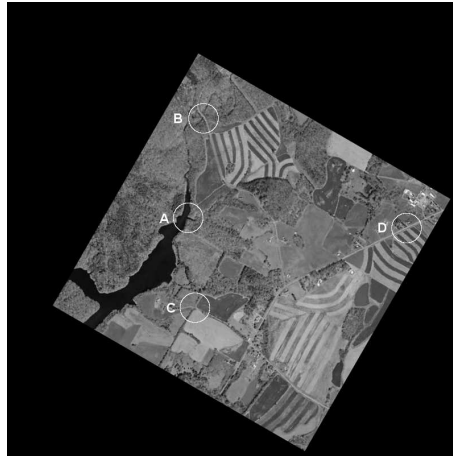
Figure 7.16: The reference image of the size 800×800 pixels, which is created by $30°$ clockwise rotation of Fig.(7.15a) and then shifted 30 pixels along x axis direction and 40 pixels along y axis direction. We selected 100 templates, four of them are displayed as examples.

Table 7.2: The number of detected templates with the matching error less than threshold E.

	Mild noise				Heavy noise			
E	2.0	4.0	6.0	8.0	2.0	4.0	6.0	8.0
GEI	65	76	78	78	62	70	72	73
GHI	95	97	99	100	91	93	93	94

where c_{pq} is a complex moment of the image. The one from GHIs has a similar form

$$\mathbf{V}_h = \Big[d_{11},\ d_{21}d_{12},\ \mathrm{Re}(d_{20}d_{12}^2),\ \mathrm{Im}(d_{20}d_{12}^2),\ \mathrm{Re}(d_{30}d_{12}^3),\ \mathrm{Im}(d_{30}d_{12}^3),\ d_{22},$$
$$\mathrm{Re}(d_{31}d_{12}^2),\ \mathrm{Im}(d_{31}d_{12}^2),\ \mathrm{Re}(d_{40}d_{12}^4),\ \mathrm{Im}(d_{40}d_{12}^4),\ d_{32}d_{23},\ \mathrm{Re}(d_{32}d_{12}),$$
$$\mathrm{Im}(d_{32}d_{12}),\ \mathrm{Re}(d_{41}d_{12}^3),\ \mathrm{Im}(d_{41}d_{12}^3),\ \mathrm{Re}(d_{50}d_{12}^5),\ \mathrm{Im}(d_{50}d_{12}^5)\Big].$$

$$(7.63)$$

During the matching the feature of a template is compared with those of the windows centered in each pixel in the degraded image. The smallest Euclidean distance in the feature space determines the matching result. Since we know the ground-truth transformation parameters, it is easy to compute the ground-truth position of each template in the degraded images. The matching error E_i of the i-th template is calculated as the distance between the center of the ground truth and that of the detected template in the degraded image. Table 7.2 shows the number of the templates the error of which was less than a given threshold E. This number is a success measure on a given level of tolerance.

The data in Table 7.2 show that the GHIs produce better matching results than the GEIs. For the image with mild degradation, GHIs can recognize 97 templates with $E < 4.0$; comparatively, GEIs just recognize 76 templates within the same error. All the templates matched by GHIs have errors below 8.0. This number is much greater than that of GEIs. In case of heavy noise, both invariants produce less satisfactory matchings. Anyway, also here GHIs outperform GEIs on all tolerance levels.

Now the centers of the corresponding templates can be used as control points (CPs) for image registration. We need to estimate the transformation parameters and then resample the image.

Although we know that there is actually no between-image scaling, we still assume a more general similarity transformation because in practice we would not know whether or not a scaling is present. Such a transformation has four parameters, so theoretically two CP pairs are sufficient to find them. Since we have 100 CP pairs, we apply standard least-square fit. We define the directional errors ex_i and ey_i for the i-th template as

$$\left(\begin{array}{c} ex_i \\ ey_i \end{array} \right) = \left(\begin{array}{cc} a & -b \\ b & a \end{array} \right) \left(\begin{array}{c} x_i \\ y_i \end{array} \right) + \left(\begin{array}{c} g \\ h \end{array} \right) - \left(\begin{array}{c} u_i \\ v_i \end{array} \right), \qquad (7.64)$$

where a, b, g and h are the parameters to be derived and (x_i, y_i) and (u_i, v_i) are the coordinates of the corresponding CPs in the sensed and reference images, respectively.

The relationship between a and b on one hand and the scaling s and rotation angle α is $a = s \cos \alpha$ and $b = s \sin \alpha$.

We minimize a sum of error squares ($N = 100$ in our case)

$$\lambda = \sum_{i=1}^{N} (ex_i^2 + ey_i^2), \tag{7.65}$$

which is done by setting partial derivatives of λ to zero

$$\frac{\partial \lambda}{\partial a} = 0, \quad \frac{\partial \lambda}{\partial b} = 0, \quad \frac{\partial \lambda}{\partial g} = 0, \quad \frac{\partial \lambda}{\partial h} = 0. \tag{7.66}$$

Eq.(7.66) leads to a linear system of equations which directly provides the unknown parameters

$$\begin{pmatrix} \sum_{i=1}^{N}(x_i^2 + y_i^2) & 0 & \sum_{i=1}^{N} x_i & \sum_{i=1}^{N} y_i \\ 0 & \sum_{i=1}^{N}(x_i^2 + y_i^2) & -\sum_{i=1}^{N} y_i & \sum_{i=1}^{N} x_i \\ \sum_{i=1}^{N} x_i & -\sum_{i=1}^{N} y_i & N & 0 \\ \sum_{i=1}^{N} y_i & \sum_{i=1}^{N} x_i & 0 & N \end{pmatrix} \times \begin{pmatrix} a \\ b \\ g \\ h \end{pmatrix}$$
$$= \begin{pmatrix} \sum_{i=1}^{N}(x_i u_i + y_i v_i) \\ \sum_{i=1}^{N}(x_i v_i - y_i u_i) \\ \sum_{i=1}^{N} u_i \\ \sum_{i=1}^{N} v_i \end{pmatrix}. \tag{7.67}$$

When registering the image in Fig.(7.15b) by means of GHIs, the above algorithm yields the parameters $a = 0.8660$, $b = 0.5001$, $g = 30.3304$, and $h = 39.7996$, which means the estimated angle of rotation is $30.006°$, the scaling is 1.00003 and translation is 30.3 pixels in x axis and 39.8 pixels in y axis. These values are almost equal to the ground truth. When we repeat the same for the GEIs, we obtain $a = 0.6873$, $b = 0.3669$, $g = 31.7804$, and $h = 31.9471$, which yield the rotation angle $28.09°$ and the scaling 0.7791. All these values are quite far from the ground truth.

This experiment illustrates that the GHIs, thanks to their stability, yield better template matching results than the traditional GEIs and hence provide more accurate estimation of registration parameters.

7.6 Conclusion

The orthogonal Gaussian–Hermite moments are introduced in this chapter. We show how to derive rotation invariants from this kind of moments in both 2D and 3D spaces. The proposed method enables us to use geometric invariants to generate Gaussian–Hermite invariants. Since geometric invariants have been systematically studied, we are able to obtain Gaussian–Hermite invariants as many as the existing geometric invariants. Moreover, we can also take advantage of the better numerical stability of the orthogonal moments in the generated invariants.

The better image representation ability is also demonstrated in comparison with exact Legendre algorithm, discrete Tchebichef and Krawtchouk moments. The experimental results show that Gaussian–Hermite moments outperform these popular moments in image reconstruction. Besides, the reconstruction can also be extended to 3D case.

The application in image registration was presented to show the potential usage of Gaussian–Hermite moments and their invariants. It indicates that Gaussian–Hermite moments and their invariants are useful tools in image processing and pattern recognition and may replace the other moments used so far in many applications.

Acknowledgement

References

[1] N. Canterakis. 3D Zernike moments and Zernike affine invariants for 3D image analysis and recognition. In *Scandinavian Conference on Image Analysis (SCIA)*, pages 85–93. DSAGM, 1999.

[2] D. Cyganski and J.A. Orr. *Object recognition and orientation determination by tensor methods*. JAI Press, Greenwich, United Kingdom, first edition, 1988.

[3] J. Fehr. Local rotation invariant patch descriptors for 3D vector fields. In *International Conference on Pattern Recognition (ICPR)*, pages 1381–1384, August 2010.

[4] J. Fehr and H. Burkhardt. 3D rotation invariant local binary patterns. In *International Conference on Pattern Recognition (ICPR)*, pages 1–4, December 2008.

[5] J. Flusser. On the independence of rotation moment invariants. *Pattern Recognition*, 33(9):1405–1410, 2000.

[6] J. Flusser, J. Boldys, and B. Zitova. Moment forms invariant to rotation and blur in arbitrary number of dimensions. *IEEE Transactions on Pattern Analysis and Machine Intelligence*, 25(2):234–246, 2003.

[7] J. Flusser, T. Suk, and B. Zitova. *Moments and Moment Invariants in Pattern Recognition*. Wiley, Chichester, United Kingdom, 2009.

[8] J.M. Galvez and M. Canton. Normalization and shape recognition of three-dimensional objects by 3D moments. *Pattern Recognition*, 26(5):667–681, 1993.

[9] X. Guo. Three dimensional moment invariants under rigid transformation. In *International Conference on Computer Analysis of Images and Patterns (CAIP)*, volume 719 of *LNCS*, pages 518–522, Budapest, Hungary, 1993.

[10] K. M. Hosny. New set of rotationally Legendre moment invariants. *International Journal of Electrical and Electronics Engineering*, 4(3):176–180, 2010.

[11] K.M. Hosny. Exact Legendre moment computation for gray level images. *Pattern Recognition*, 40(12):3597–3605, 2007.

[12] M.K. Hu. Visual pattern recognition by moment invariants. *IRE Transactions on Information Theory*, 8(2):179–187, 1962.

[13] R. Kakarala and D. Mao. A theory of phase-sensitive rotation invariance with spherical harmonic and moment-based representations. In *IEEE Conference on Computer Vision and Pattern Recognition (CVPR)*, pages 105–112, June 2010.

[14] M. Kazhdan. An approximate and efficient method for optimal rotation alignment of 3D models. *IEEE Transactions on Pattern Analysis and Machine Intelligence*, 29(7):1221–1229, 2007.

[15] M. Kazhdan, T. Funkhouser, and S. Rusinkiewicz. Rotation invariant spherical harmonic representation of 3D shape descriptors. In *Eurographics/ACM SIG-GRAPH symposium on Geometry processing (SGP)*, pages 156–164, Aire-la-Ville, Switzerland, June 2003. Eurographics Association.

[16] A. Khotanzad and Y.H. Hong. Invariant image recognition by Zernike moments. *IEEE Transactions on Pattern Analysis and Machine Intelligence*, 12(5):489–497, 1990.

[17] Y.J. Li. Reforming the theory of invariant moments for pattern recognition. *Pattern Recognition*, 25(7):723–730, 1992.

[18] C.H. Lo and H.S. Don. 3-D moment forms: Their construction and application to object identification and positioning. *IEEE Transactions on Pattern Analysis and Machine Intelligence*, 11(10):1053–1064, 1989.

[19] J.F. Mangin, F. Poupon, E. Duchesnay, D. Riviere, A. Cachia, D.L. Collins, A.C. Evans, and J. Regis. Brain morphometry using 3D moment invariants. *Medical Image Analysis*, 8(3):187–196, 2004.

[20] R. Mukundan. Some computational sspects of discrete orthonormal moments. *IEEE Transactions on Image Processing*, 13(8):1055–1059, 2004.

[21] County Orange. Aerial image sample, 2012. [online] - Available: http://www.co.orange.nc.us/soilwater/AerialPhotos.asp.

[22] Princeton. Princeton Shape Benchmark, 2013. [online] - Available: http://shape.cs.princeton.edu/benchmark/.

[23] T.H. Reiss. *Recognizing planar objects using invariant image features*. Springer-Verlag, Berlin, Germany, first edition, 1993.

[24] F A. Sadjadi and E.L. Hall. Three-Dimensional moment invariants. *IEEE Transactions on Pattern Analysis and Machine Intelligence*, PAMI-2(2):127–136, 1980.

[25] H. Skibbe, M. Reisert, and H. Burkhardt. SHOG-Spherical HOG descriptors for rotation invariant 3D object detection. In R. Mester and M. Felsberg, editors, *Deutsche Arbeitsgemeinschaft für Mustererkennung (DAGM)*, volume 6835 of *LNCS*, pages 142–151. Springer Berlin Heidelberg, 2011.

[26] T. Suk and J. Flusser. Tensor method for constructing 3D moment invariants. In *International Conference on Computer Analysis of Images and Patterns (CAIP)*, volume 6855 of *LNCS*, pages 212–219, Seville,Spanien, 2011.

[27] T. Suk and J. Flusser. 3D rotation invariants, 2012. [online] - Available: http://zoi.utia.cas.cz/3DRotationInvariants.

[28] M. Trummer, H. Suesse, and J. Denzler. Coarse registration of 3D surface triangulations based on moment invariants with applications to object alignment and identification. In *International Conference on Computer Vision (ICCV)*, pages 1273–1279, October 2009.

[29] A. Wallin and O. Kubler. Complete sets of complex Zernike moment invariants and the role of the pseudoinvariants. *IEEE Transactions on Pattern Analysis and Machine Intelligence*, 17(11):1106–1110, 1995.

[30] Wikipedia. Euler angles, 2012. [online] - Available: http://en.wikipedia.org/wiki/Euler_angles.

[31] W.H. Wong, W.C. Siu, and K.M. Lam. Generation of moment invariants and their uses for character recognition. *Pattern Recognition Letters*, 16(2):115–123, 1995.

[32] D. Xu and H. Li. Geometric moment invariants. *Pattern Recognition*, 41(1):240–249, 2008.

[33] B. Yang and M. Dai. Image analysis by Gaussian–Hermite moments. *Signal Processing*, 91(10):2290–2303, 2011.

[34] B. Yang and M. Dai. Image reconstruction from continuous Gaussian–Hermite moments implemented by discrete algorithm. *Pattern Recognition*, 45:1602–1616, 2012.

[35] B. Yang, J. Flusser, and T. Suk. 3D rotation invariants of Gaussian–Hermite moments. *submitted to Pattern Recognition Letters*.

[36] B. Yang, G. Li, H. Zhang, and M. Dai. Rotation and translation invariants of Gaussian–Hermite moments. *Pattern Recognition Letters*, 32(9):1283–1298, 2011.

[37] P.T. Yap, R. Paramesran, and S.H. Ong. Image analysis by Krawtchouk moments. *IEEE Transactions on Image Processing*, 12(11):1367–1377, 2003.